De Novo Designed Self-Assembling Rhodamine Probe for Real-Time, Long-Term and Quantitative Live-Cell Nanoscopy

Jie Zhang,[△] Heng Shi,[△] Chen Huang, Le Mei, Qiang Guo, Ke Cheng, Pingzhou Wu, Dan Su, Qingxin Chen, Shenglong Gan, Cecilia Ka Wing Chan, Jiahai Shi, Jian Lin Chen, Chung Hang Jonathan Choi, Shao Q. Yao, Xian-Kai Chen, Ben Zhong Tang, Jufang He,* and Hongyan Sun*

Read Online

ACCESS | Metrics & More | Article Recommendations | Supporting Information

ABSTRACT: Super-resolution imaging provides a powerful approach to image dynamic biomolecule events at nanoscale resolution. An ingenious method involving tuning intramolecular spirocyclization in rhodamine offers an appealing strategy to design cell-permeable fluorogenic probes for super-resolution imaging. Nevertheless, precise control of rhodamine spirocyclization presents a significant challenge. Through detailed study of the structure−activity relationship, we identified that multiple key factors control rhodamime spirocyclization. The findings provide opportunities to create fluorogenic probes with tailored properties. On the basis of our findings, we constructed self-assembling rhodamine probes for no-wash live-cell confocal and super-resolution imaging. The designed self-assembling probe Rho-2CF3 specifically labeled its target proteins and displayed high ring-opening ability, fast labeling kinetics (<1 min), and large turn-on fold (>80 folds), which is very difficult to be realized by the existing methods. Using the probe, we achieved high-contrast super-resolution imaging of nuclei and mitochondria with a spatial resolution of up to 42 nm. The probe also showed excellent photostability and proved ideal for real-time and long-term tracking of mitochondrial fission and fusion events with high spatiotemporal resolution. Furthermore, Rho-2CF3 could resolve the ultrastructure of mitochondrial cristae and quantify their morphological changes under drug treatment at nanoscale. Our strategy thus demonstrates its usefulness in designing self-assembling probes for super-resolution imaging.

KEYWORDS: *rhodamine spirocyclization, self-assembly, fluorogenic probes, self-labeling tag, live-cell imaging, super-resolution microscopy*
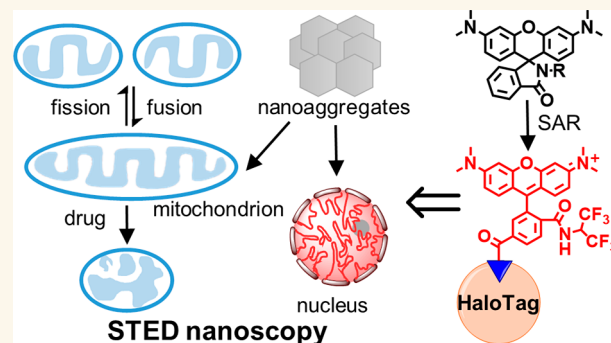
S uper-resolution microscopy has emerged as a powerful imaging tool to explore dynamic biomolecule events at nanoscale. Further advances in super-resolution imaging rely on the creation of diverse small-molecule fluorophores.[1] Among the different fluorophores, rhodamine derivatives have shown high brightness, excellent photostability, and biocompatibility. They have thus become the most important class of fluorophores for live-cell imaging.[2−4] An interesting property of rhodamine-based fluorophores is their intramolecular spirocyclization behavior between a nonfluorescent lactone and fluorescent zwitterion form (Figure 1A). Tuning the spirocyclization equilibrium provides an appealing strategy for designing cell-permeable fluorogenic probes for intracellular labeling of proteins.[5] In one strategy, replacing the oxygen-bridge in rhodamines with electron-deficient atom or group (C or Si)

dramatically reduces the tendency for ring opening and allows for the creation of highly fluorogenic probes.[6−16] A representative example is silicon rhodamine (SiR), which serves as a highly popular scaffold for super-resolution imaging.[6−11] Recently, Lavis et al. developed "Janelia Fluor" (JF) dyes with the far-red property by fine-tuning the sulfur, phosphinate, phosphine oxide, or sulfone substituted rhodamines.[16] On the
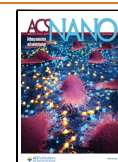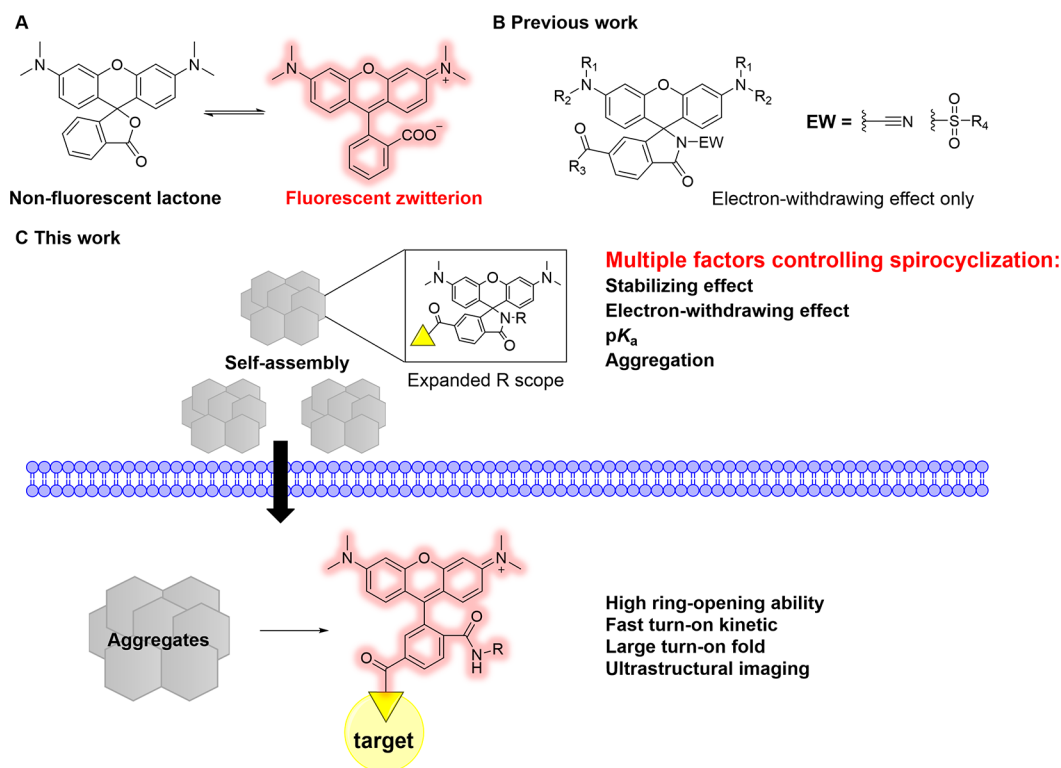
Figure 1. Design strategies for high-performance probes based on rhodamine spirolactam scaffolds. (A) Intramolecular spirocyclization equilibrium of rhodamines between nonfluorescent spirolactone and fluorescent zwitterion. (B) Previous strategies to develop rhodamine-based fluorogenic probes focusing on electron-withdrawing effect. (C) Strategy in our work to develop self-assembling rhodamine probes with expanded substrate scope. It leads to deep insights into the controlling mechanism of spirocyclization and the creation of high-performance fluorophores for super-resolution imaging.

other hand, increasing the electron-withdrawing strength in the amino group or the fluorination of the fluorophore core of rhodamine also favors lactone ring closure and enables super-resolution imaging.[12,14−16] A seminal work has seen the use of 3-substituted azetidine groups to fine-tune fluorophores by Lavis et al.[15] Nevertheless, the above modifications are based on reducing the electron density of the xanthene core, which may affect the spectroscopic or chemical properties of the fluorophore, such as reduced quantum yield, changes in absorbance and emission spectra, or decreased stability in cellular environment.[13,16−20] Furthermore, the chemical modification of xanthene core usually requires tedious synthesis, making such approaches inaccessible to most laboratories.

In a recent pioneering work, Johnsson et al. developed an ingenious strategy to control rhodamine spirocyclization by introducing an electron-withdrawing amide to develop fluorogenic probes (Figure 1B).[21] The method has been shown to transform regular rhodamine fluorophores into fluorogenic probes with good cell permeability. Very recently, they extended their work to transform the same rhodamine dye into either a fluorogenic probe or a spontaneously blinking dye.[22] Nevertheless, these strategies have focused mainly on modulating the electron-withdrawing ability of substituents in rhodamines, and the exploration and optimization of rhodamine spirocyclization by other factors is very limited.

Herein, we systematically interrogated the intramolecular spirocyclization switching mechanism by judiciously designing a library of rhodamine spirolactams with diverse substitution patterns at the spirocyclic ring (Figure 1C). Through a detailed structure−activity relationship study, we gained deep insights into various key factors contributing to the switching mechanism

of intramolecular spirocyclization: 1. Low pK_a of rhodamines and aggregate formation are predominant factors for minimizing fluorescence background. 2. Stabilizing effects such as resonance delocalization/intramolecular hydrogen bond play crucial roles in stabilizing fluorescent zwitterions and promoting the ring-opening process. 3. Incorporation of an electron-withdrawing group at the spirocyclic ring accelerates the ring-opening rate. On the basis of these important findings, we successfully designed high-performance self-assembling probes that simultaneously possess high ring-opening ability, fast turn-on kinetics, and large turn-on fold. Such probes are difficult to be realized by the existing methods. The probes were successfully applied to high-contrast imaging applications with no-wash, live-cell, time-lapse confocal and stimulated emission depletion (STED) imaging.

RESULTS AND DISCUSSION

Structure−Activity Relationship Study on Intramolecular Spirocyclization. Tuning the dynamic equilibrium between nonfluorescent lactone/lactam and fluorescent zwitterion forms is vital for designing rhodamine probes with high fluorogenicity. We first investigated the spirocyclization switching mechanism by synthesizing a library of rhodamine spirolactams **1−15** with diverse substitution patterns at the spirocyclic ring of rhodamine B (RhoB) (Figure 2A). RhoB was chosen in our platform as it is widely used and possesses excellent photophysical properties. A control fluorophore **9** with the reported sulfonamide moiety was incorporated for comparison. The rhodamine spirolactam fluorophores **1−15** were obtained by coupling RhoB with the corresponding amines
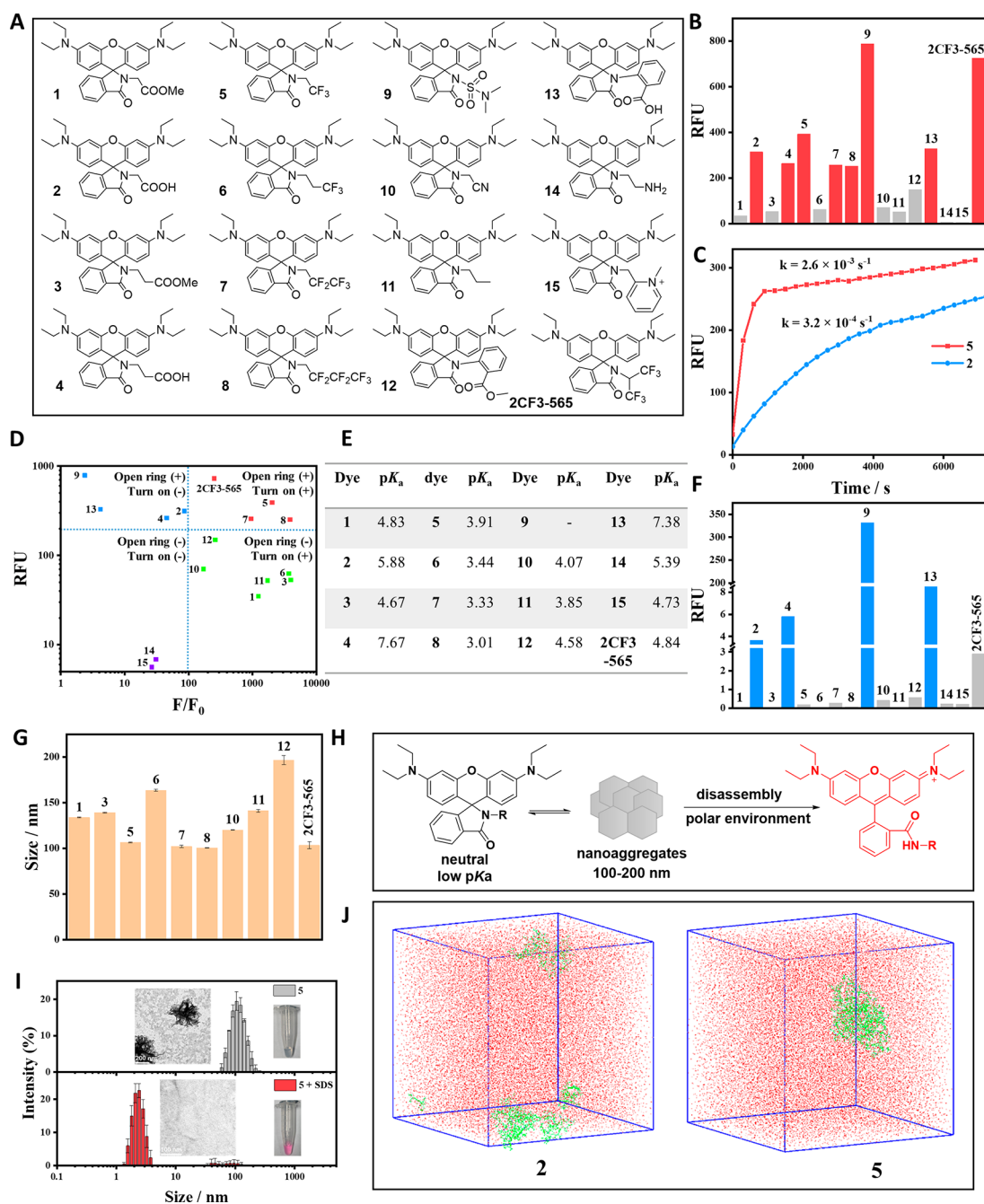
Figure 2. Structure−activity relationship study of rhodamine spirolactams. (A) Modular design structures of the rhodamine spirolactams (1−15, 2CF3-565). (B) Fluorescence intensity of 1−15, 2CF3-565 (5 μM) after treatment with 0.4% SDS. (C) Ring-opening kinetic test of 2, 5 (5 μM) upon addition of 0.4% SDS. (D) Plot of the fluorescence intensity of rhodamines versus the turn-on fold after SDS treatment. (E) Summary of the pK_a values of 1−15, 2CF3-565. (F) Fluorescence background of 1−15, 2CF3-565 (5 μM) in HEPES buffer (pH = 7.3). (G) The nanoaggregate size of corresponding rhodamine spirolactams (5 μM) in HEPES buffer (pH = 7.3). (H) Aggregation and disassembly process of spirolactams. (I) The nanoaggregate size of 5 (5 μM) measured by DLS before and after treatment of 0.4% SDS. Inset showed the TEM images and the color changes observed by naked eye. (J) Molecular dynamic simulations of 2, 5 in water to study their aggregation behavior.

and subsequently subjecting it to hydrolysis (for 2, 4, 13), deprotection (for 14), and methylation (for 15). The rhodamine spirolactams were unambiguously characterized by ^{1}H nuclear magnetic resonance (NMR), ^{13}C NMR, and mass spectrometry, respectively.

With these rhodamine spirolactams in hand, we first investigated their ring-opening properties. Anionic surfactants such as sodium dodecyl sulfate (SDS) have been shown to induce the ring-opening of rhodamine spirolactams.[6,13,21] Briefly

the rhodamine spirolactams were incubated with 0.4% SDS, and their fluorescence was measured accordingly (Figures 2B, S1). As expected, the control fluorophore 9 bearing a sulfonamide group showed strong fluorescence after SDS treatment. This is presumably due to the stabilization of fluorescent zwitterion by electron-withdrawing sulfonamide through both induction and resonance effects. Interestingly, carboxylic acid-containing spirolactams 2, 4, and 13 also showed high fluorescence after SDS treatment, and the fluorescence signals were much stronger

than those of their esterified counterparts **1**, **3**, and **12**, implying that intramolecular hydrogen bonding contributes to the stabilization of fluorescent zwitterions. A recent super-resolution imaging study revealed that a carboxylate group in rhodamine could stabilize the photoactivated zwitterionic structure through hydrogen bonding, supporting our hypothesis.[23] Surprisingly, β-fluorine-containing spirolactams **5**, **7**, and **8** exhibited enhanced ring-opening ability. As the CF_3 group has been reported to form a hydrogen bond with the NH group, we surmise that intramolecular hydrogen bond can be formed between CF_3 and NH in rhodamines and significantly promotes the ring-opening process.[24] In contrast, γ-fluorine-containing spirolactam **6** showed a relatively low fraction of opened spirolactams, highlighting the importance of β-fluorine for the stabilizing effects. These results collectively suggest that the stabilizing effect such as resonance delocalization/hydrogen bond plays crucial roles in controlling the ring-opening ability.

Further bovine serum albumin (BSA) testing showed that all the rhodamine spirolactams had little fluorescence change upon the addition of BSA (Figure S1), demonstrating that rhodamine spirolactam structure could avoid the interference of nonspecific interaction. In addition, the ring-opening rate was found to be positively correlated with the electron-withdrawing effect, since the ring-opening rate of **5** ($k = 2.6 \times 10^{-3}$ s^{-1}) with a trifluoromethyl group is about 1 order of magnitude faster than that of **2** ($k = 3.2 \times 10^{-4}$ s^{-1}) with a carboxylic acid group (Figure 2C). On the other hand, hydrophobicity seems to be unfavored for the ring-opening kinetics, as evidenced from the ring-opening rates of **5**, **7**, and **8** in Figure S2 (hydrophobicity: **5** < **7** < **8**; ring-opening rate: **5** > **7** > **8**).

We next investigated the turn-on fold of these rhodamine spirolactams, an instrument property for determining their fluorogenicity and suitability for no-wash imaging. The relationship between the ring-opening ability and the turn-on fold of the rhodamine spirolactams was plotted in Figure 2D. The rhodamine spirolactams were grouped with the following criteria (relative fluorescence unit (RFU) > 200: high ring-opening ability, Open ring (+); RFU ≤ 200: low ring-opening ability, Open ring (−); turn-on fold >100: high turn-on fold, Turn on (+); turn-on fold ≤100: low turn-on fold, Turn on (−)). Specifically, we could categorize these spirolactams into four groups: (1) **5**, **7**, and **8** with high ring-opening ability and high turn-on fold; (2) **2**, **4**, **9**, and **13** with high ring-opening ability and low turn-on fold; (3) **14** and **15** with low ring-opening ability and low turn-on fold; (4) **1**, **3**, **6**, **10**, **11**, and **12** with low ring-opening ability and high turn-on fold. Among all the rhodamine spirolactams, **9** shows the highest ring opening ability, but the turn-on fold is low. In contrast, **5**, **7**, and **8** possess high ring-opening ability and high turn-on fold simultaneously, making them highly suitable for constructing fluorogenic probes.

Further data analysis revealed that the turn-on fold is not only determined by the ring-opening ability but also heavily dependent on the background in aqueous buffer (pH = 7.3). To gain insight into the factors controlling background, we studied the pK_a of these rhodamine spirolactams in an aqueous environment (Figure S3). Interestingly, a positive correlation between pK_a and background could be found (Figure 2E and 2F). For example, the carboxylic acid containing spirolactams **2**, **4**, and **13** showed relatively higher pK_a, i.e. 1 pH unit higher than other spirolactams. Accordingly, these fluorophores all showed relatively higher background than other spirolactams and exhibited low turn-on fold (Figure 2F). On the other hand, spirolactam **9** with resonance structure showed a reversible pH

titration behavior and always-on property in neutral and basic solutions (Figure S3). This fluorophore also results in high background and low turn-on fold. In contrast, **5**, **6**, **7**, and **8**, which contain a −CF_3 moiety, displayed a significantly low pK_a and weak fluorescence background. These results together suggest that a low pK_a value is highly essential for a low background and large turn-on fold.

Apart from pK_a, aggregation behavior can also affect the background of rhodamine spirolactams.[13] However, its detailed mechanism remains unclear. We next investigated the aggregation behavior of these rhodamine spirolactams **1**−**15**. As shown in Figure S4, DLS results revealed that charged spirolactams **2**/**4**/**13**/**14**/**15** and **9** could hardly form uniform aggregation. This could be attributed to the charge repulsion or high ratio of opened ring structures, rendering these fluorophores unfavored to self-assemble to form nanoaggregates. On the other hand, neutral spirolactams with a low pK_a, e.g. **5**/**6**/**7**/**8**, were found to form uniform nanoaggregates of 100−200 nm (Figure 2G and 2H). This further contributes to their low fluorescence background and high fluorogenicity upon disassembly in polar environment. Moreover, the disaggregation process of these spirolactams after SDS treatment was unambiguously confirmed by TEM and DLS measurements (Figures 2I, S5).

Intrigued by the low background of CF_3-containing **5**/**6**/**7**/**8**, we further performed molecular dynamics (MD) simulations to investigate the aggregation behavior of rhodamine spirolactams at the molecular level. A representative compound **5** was selected in our study. Interestingly, **5** was found to form large and uniform nanoaggregates in the MD study. In contrast, **2** was found to form less and inhomogeneous nanoaggregates under the same conditions (Figure 2J), illustrating the distinct aggregation behavior caused by different structures of rhodamines. Collectively, these results elucidated the underlying self-aggregation mechanism of rhodamine spirolactams and provided a solid basis to clarify their low background caused by aggregation. In other words, introducing charged groups or increasing the pK_a of rhodamine spirolactams can serve as a general design principle to preclude aggregation of these fluorophores.

Through the above detailed structure−activity relationship (SAR) analysis, we gained an in-depth understanding of the various factors contributing to the ring-opening process of rhodamines. A stabilizing effect such as resonance delocalization/hydrogen bonding contributes to the stabilization of fluorescent zwitterions upon SDS binding. The introduction of a strong electron-withdrawing group accelerates the kinetics of ring opening. Low pK_a and aggregate formation, on the other hand, lead to a low fluorescence background of rhodamines. Fine-tuning these factors provides valuable approaches to design high-performance rhodamine fluorophores with high ring-opening ability, fast turn-on kinetics, and large turn-on fold. Based on the above considerations, 1,1,1,3,3,3-hexafluoropro-pan-2-amine-modified spirolactam **2CF3-565** was further designed for the following reasons: (1) An extra β-fluorine group is incorporated to improve stabilization effects and enhance ring-opening ability. (2) The electron-withdrawing effect is increased to accelerate ring-opening rate. (3) The scaffold is designed with a low pK_a and neutral charge to allow aggregate formation to minimize background. As expected, **2CF3-565** exhibited extremely high ring-opening ability (RFU > 720), large turn-on fold (251-fold), very fast turn-on kinetics ($k = 2.9 \times 10^{-2}$ s^{-1}), low pK_a (4.84), and self-assembling ability
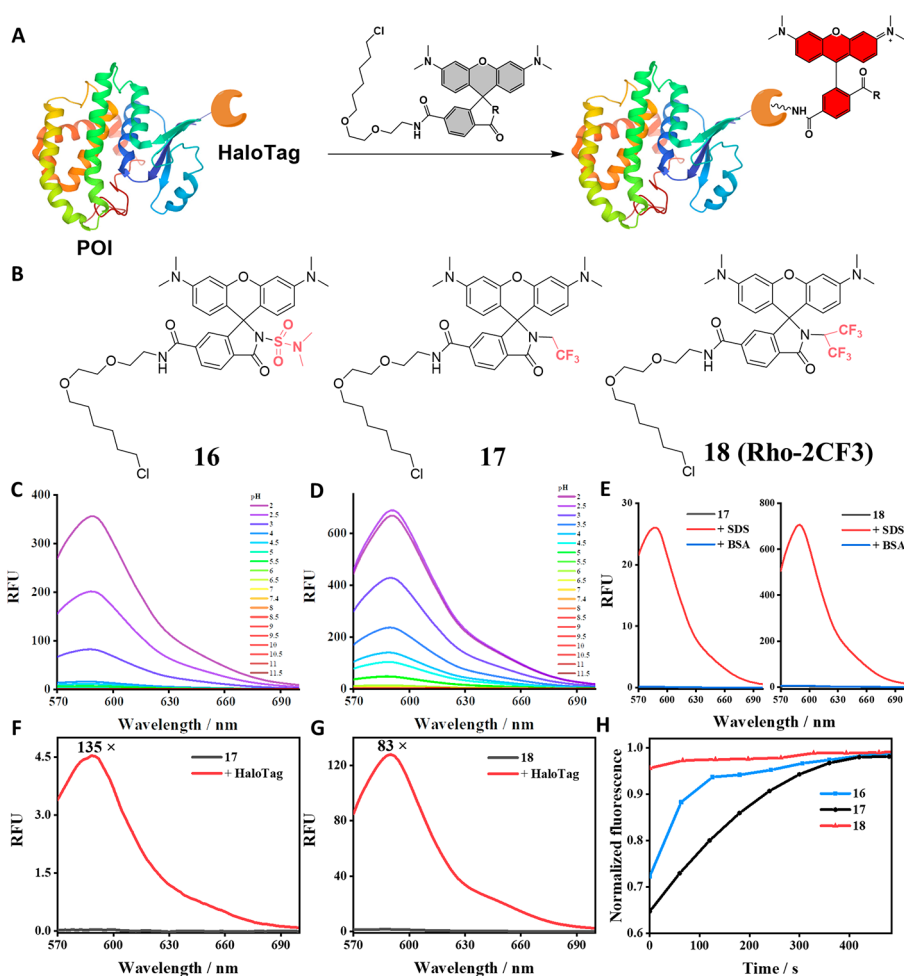
Figure 3. High-performance self-assembling probes for HaloTag labeling. (A) Mechanism of rhodamine-based probes for labeling HaloTag proteins. (B) Chemical structure of the probes. (C, D) pH titration spectra of 17 and 18 (5 μM). (E) Fluorescent spectra change of 17 or 18 (5 μM) before and after incubation with 0.4% SDS or 0.4% BSA in HEPES buffer (pH = 7.3). (F, G) Fluorescence spectra change of 17 or 18 (2.5 μM) before and after incubation with HaloTag7 (5 μM) in HEPES buffer (pH = 7.3). (H) Labeling kinetic test of 16−18 (1 μM) with HaloTag7 (1.68 μM) in HEPES buffer (pH = 7.3).

(size 103.4 nm) (Figures 2, S6). These results firmly confirmed that our strategy can yield high-performance fluorophores for bioimaging applications.

HaloTag Fusion Protein Labeling with High-Performance Rhodamine Probes. HaloTag is a widely used self-labeling protein tag that provides an efficient method for intracellular fluorescent labeling of proteins (Figure 3A).[25] Fluorogenic probes for HaloTag labeling are valuable tools compatible with no-wash live-cell imaging.[26] Based on the aforementioned SAR study, we sought to design high-performance self-assembling probes with optimized rhodamine scaffolds. 2,2,2-Trifluoroethyl amine and 1,1,1,3,3,3-hexafluoropropan-2-amine modified spirolactams were selected in our study as the fluorophores showed a large turn-on fold and good ring-opening ability.

To synthesize the probes, 6-carboxytetramethyl-rhodamine (6-TAMRA) was coupled to the chloroalkane amine (CA) linker to afford the intermediate **19** (Scheme S2). Amidation of **19** with corresponding amines then afforded probes **16** (**MaP555-Halo**), **17**, and **18** (**Rho-2CF3**) respectively (Figure 3B). Probe **16** was synthesized as a control for comparison study. The photophysical properties (Table S1) and chemical stability (Figure S7) of the probes were first investigated. The results showed that the photophysical properties of the open-

ring forms of probes are similar to those of the parent parent fluorophore RhoB. The probes also exhibited high chemical stability toward various reactive species such as H_2O_2, ClO^-, etc. As expected, both **17** and **18** showed low pK_a values (2.60 for **17** and 3.25 for **18**) and formed nanoaggregates in aqueous solution (Figures 3C, 3D, S8−S10), ensuring a very low fluorescence background of both probes. However, the control probe **16** showed an "always on" property from pH 2 to 12 in pH titration experiments. In addition, no obvious nanoaggregates were observed, resulting in its relatively high fluorescence background (Figures S8−S10). A significant fluorescence enhancement was observed for both **17** and **18** when SDS was added (Figure 3E) whereas the turn-on fold for **16** was much smaller (Figure S11A). The fluorescence intensity of **18** was even much higher than that of **17**, demonstrating its superior ring-opening ability as designed. The reduced ring-opening ability of **17** compared to the parent fluorophore **5** might be due to the decreased electron-donating ability of dimethylamine or the introduction of the HaloTag group. Furthermore, the interference of nonspecific interactions of probes was tested by adding BSA. The result showed that BSA treatment caused negligible fluorescence change of the probes, indicating that no nonspecific interference occurred.
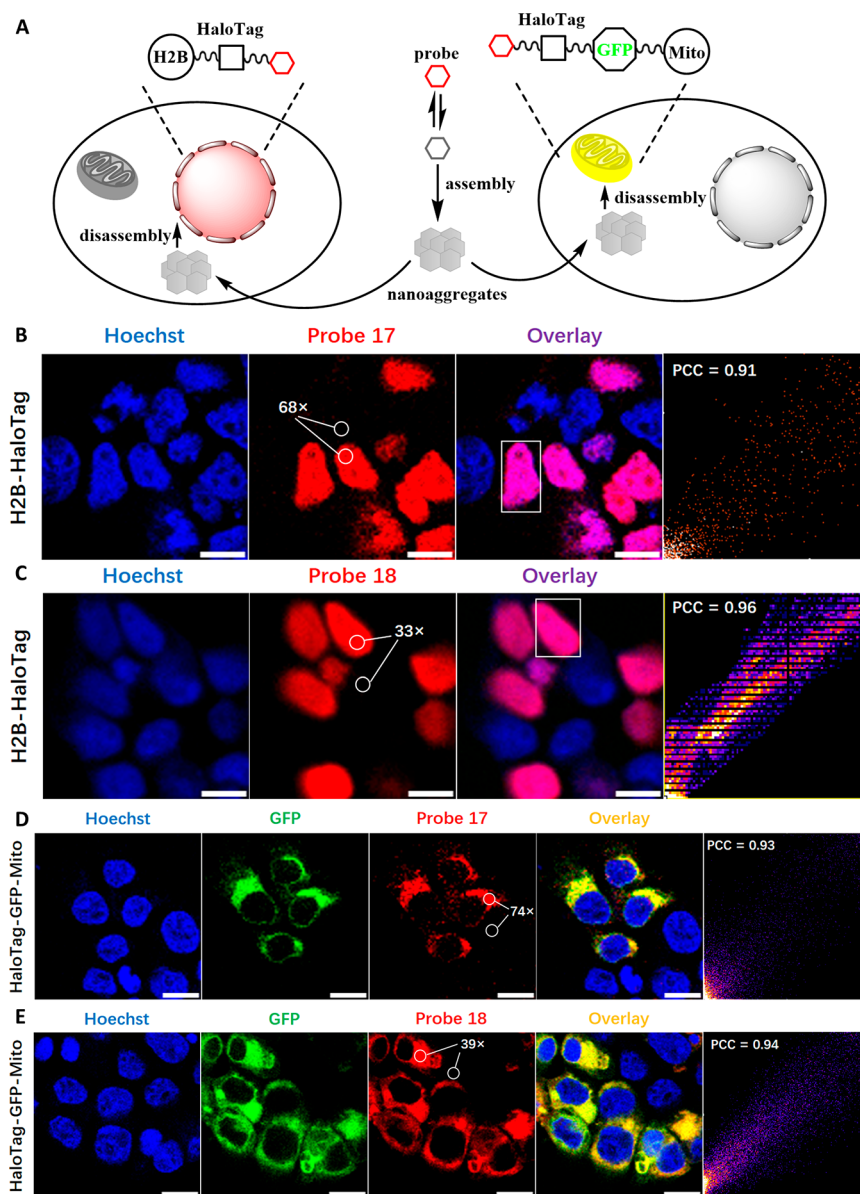
Figure 4. High-performance self-assembling probes for no-wash live-cell imaging. (A) Scheme showing the labeling of H2B-HaloTag or HaloTag-GFP-Mito by probes in HEK 293T cells. (B, C) No-wash live-cell confocal imaging of H2B-HaloTag using 17 (1 μM, B) or 18 (1 μM, C). (D, E) No-wash live-cell confocal imaging of HaloTag-GFP-Mito using 17 (1 μM, D) or 18 (1 μM, E). Hoechst channel: Ex: 405 nm, Em: 420−475 nm; GFP channel: Ex: 488 nm, Em: 500−530 nm; probe channel: Ex: 532 nm, Em: 550−620 nm. Scale bar: 10 μm.

Next we used **16**, **JF525-Halo** and **17**, **18** to detect HaloTag7 protein in HEPES buffer (pH = 7.3). In fluorescence tests with HaloTag7 (Figure 3F, 3G), both **17** and **18** showed large fluorescence turn-on folds (135-folds for **17**; 83-folds for **18**), which is much higher than that of **16** (Figure S11B) and **JF525-Halo** (Figure S12). Although the turn-on fold of **17** was higher than that of **18**, **18** showed much higher fluorescence intensity (47-folds) than **17**. This observation was consistent with the fluorescence test of SDS. In the kinetic test, **16** and **17** already exhibited very fast reaction kinetics. It took 300 and 400 s for **16** and **17** to reach the maximum fluorescence intensity respectively (Figure 3H). **18** showed even faster kinetics than **16** and **17**, suggesting its extremely fast turn-on rate (Figures 3H, S13). We reasoned that the large turn-on fold and fast reaction kinetics of the probes were attributed not only to the high affinity between HaloTag and CA ligand[27] but also to the superior ring-opening ability of the optimized rhodamine scaffolds.

High-Contrast No-Wash Live-Cell Imaging. Inspired by the high fluorogenic property of **17** and **18** in aqueous buffer, we next explored their potential ability in no-wash live-cell imaging. We hypothesize that the self-assembling probes can cross the cell membrane efficiently and bind to the target protein with high fluorescence turn on in living cells. HEK 293T cells transfected with histone 2B-HaloTag (H2B-HaloTag) or HaloTag-GFP-Mito were incubated with **17** and **18** and then imaged with confocal microscopy under no-wash conditions (Figure 4A). Both **17** and **18** enabled high-contrast imaging of the target HaloTag fusion protein in the nucleus (F_{nuc}/F_{cyt} = 68 for **17**, F_{nuc}/F_{cyt} = 33 for **18**) and mitochondria (F_{mit}/F_{cyt} = 74 for **17**, F_{mit}/F_{cyt} = 39 for **18**) compared with the cytosolic background (Figure 4B−4E). A general observation was that **18** showed higher brightness than **17**. Thus, a relatively lower concentration of **18** could be used in cell imaging experiments. Further colocalization analysis revealed that **17** and **18** stained their
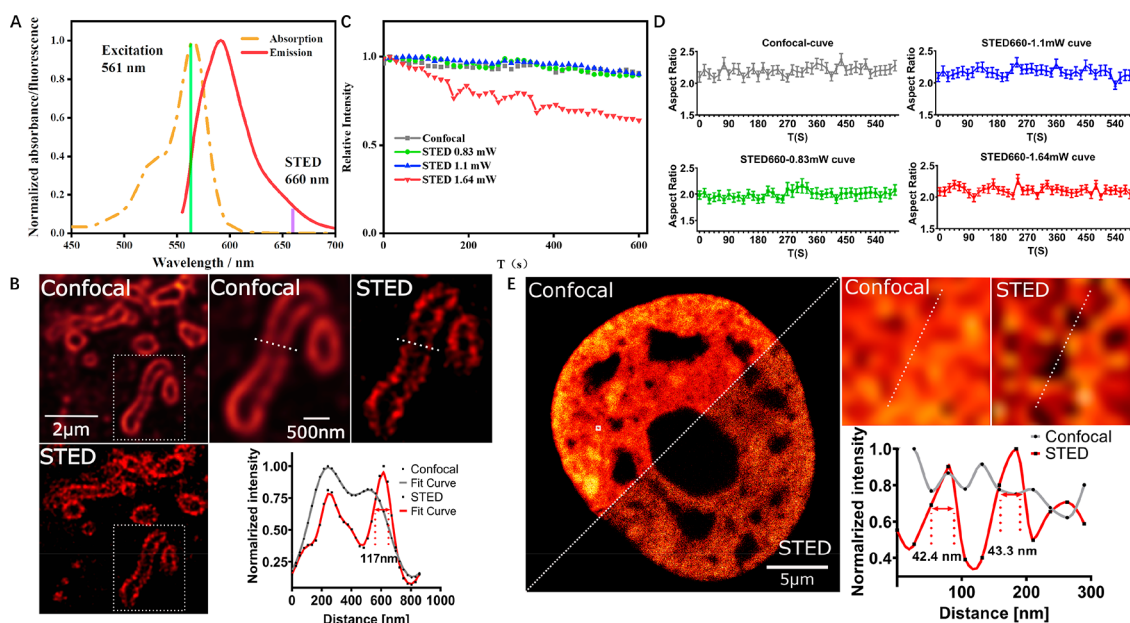
Figure 5. No-wash live-cell STED imaging. (A) Absorption and emission spectra of **18**. (B) Deconvoluted confocal and STED imaging of HeLa cells expressing HaloTag-GFP-Mito incubated with 0.5 μM **18** for 1 h. The top right images show the magnified deconvoluted confocal and STED images of the region in the white dashed box in the left panel. The bottom right figure shows a line profile across the dotted line in the top right images. The FWHM values are shown below the fitted curves. (C) Photostability study of **18** under confocal or STED imaging with different laser power. (D) Changes in mitochondrial aspect ratio under confocal imaging or STED imaging with different laser power. Error bars represent the standard deviation of the means, $n = 70-213$ mitochondria. (E) Deconvoluted confocal and STED imaging of HeLa cells expressing histone H2B-HaloTag incubated with 0.5 μM **18** for 1 h. The top right images show zoom-in deconvoluted confocal and STED images of the region in the white dotted box in the left panel. The bottom right figure shows a line profile across the dotted line in the top right images. The FWHM values are shown below the fitted curves.

target proteins with high selectivity. The Pearson coefficient values were calculated to be higher than 0.90 in all colocalization studies. This result was also collaborated by the Structural SIMilarity (SSIM) analysis (Figure S14, SSIM index = 0.911 for **17**; SSIM index = 0.861 for **18**). In addition, live-cell imaging experiments also verified that **18** has much better fluorescence turn-on ability than the control probes (**16** and **JF525-Halo**) (Figure S15). Importantly, such no-wash imaging could also be performed at various concentrations of **17** or **18** (Figures S16, S17). For example, even a high concentration of **17** and **18** (e.g., 4−5 μM) did not cause a blurred signal, implying that **17** and **18** possess an extremely low fluorescence background. Furthermore, **18** showed very fast labeling kinetics in live-cell imaging consistent with *in vitro* tests. When 0.5 μM **18** was added to cells, a significant fluorescence enhancement could be readily observed within 5 min (Figure S18). These results firmly demonstrated that the HaloTag probes **17** and **18** developed from optimized rhodamine spirolactams maintain high-performance fluorogenic properties, and they are ideal tools for high-contrast no-wash imaging of HaloTag fusion proteins in live cells.

High-Contrast Live-Cell STED Imaging. We next carried out a high-contrast live-cell STED imaging study. **18** was chosen for STED imaging[28] as it showed high ring-opening ability and fast turn-on kinetics. **18** exhibited maximum absorption at 565 nm and an emission peak at 586 nm in the open ring form. A 660 nm laser was thus selected for depletion in STED imaging (Figure 5A). The fluorescence brightness of the open-ring form of **18** was determined to be 4.03×10^4 M^{-1} cm^{-1} in aqueous solution, showing that **18** is a bright fluorophore and is suitable for STED imaging.

We first used **18** for STED imaging of the mitochondria in live cells. HeLa cells were transfected with HaloTag-GFP-Mito, stained with **18**, and directly imaged with STED microscopy. STED imaging results showed that mitochondria could be specifically stained at a low concentration of **18**, i.e. 0.5 μM. The structure of the outer mitochondrial membrane (OMM) was resolved by STED image with a full width at half-maximum (FWHM) resolution of 117 nm (Figure 5B). Further decorrelation analysis revealed a 2.29-fold resolution improvement of STED imaging (resolution = 115.6 nm) over confocal imaging (resolution = 264.6 nm) (Figure S19). Subsequently, the superior photostability of **18** was confirmed when mitochondria were imaged under a focused laser during STED imaging. **18** showed better photostability than that of control probes (**16** and **JF525-Halo**) under the same STED imaging conditions (Figure S20). The fluorescence of **18** exhibited nearly 70% survival after collecting 40 frames (15 s/frame) even under 1.64 mW STED (Figure 5C). Importantly, the low STED power applied in our experiments caused negligible photodamage of mitochondria while maintaining high resolution (Figure 5D). These results demonstrate that **18** is capable of imaging photosensitive mitochondria in live cells by STED.

Further STED imaging study with a cell nucleus showed that 0.5 μM **18** could specifically stain the nuclei of HeLa cells expressing H2B-HaloTag. After optimization, the best resolution of the nucleus nanostructure can reach as low as 42.4 nm (Figure 5E). The decorrelation analysis also showed a 2.67-fold resolution improvement by STED (Figure S21). Taking these results together, **18** has proven to be a superior fluorogenic probe for no-wash live-cell STED imaging with outstanding properties such as high brightness, good photostability, low photodamage, and high resolution.
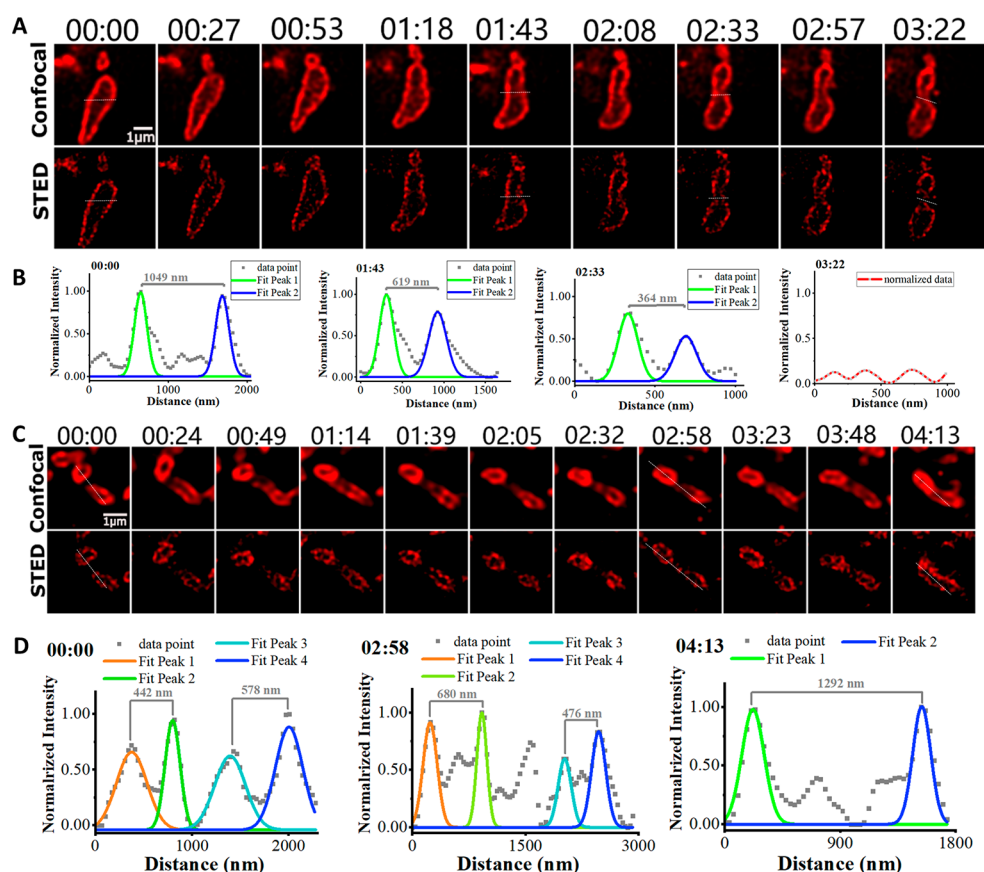
Figure 6. STED Imaging of mitochondrial fission and fusion processes. HeLa cells expressing HaloTag-GFP-Mito was used. (A, C) Time-lapse deconvoluted confocal and STED imaging of mitochondrial fission process (A) and fusion process (C). Scale bar: 1 μm. (B) Normalized intensity profile across the corresponding dotted line indicated in the deconvoluted STED images of A. (D) Normalized intensity profile across the corresponding dotted line indicated in the deconvoluted STED images of C. Time points in each image are in minutes:seconds.
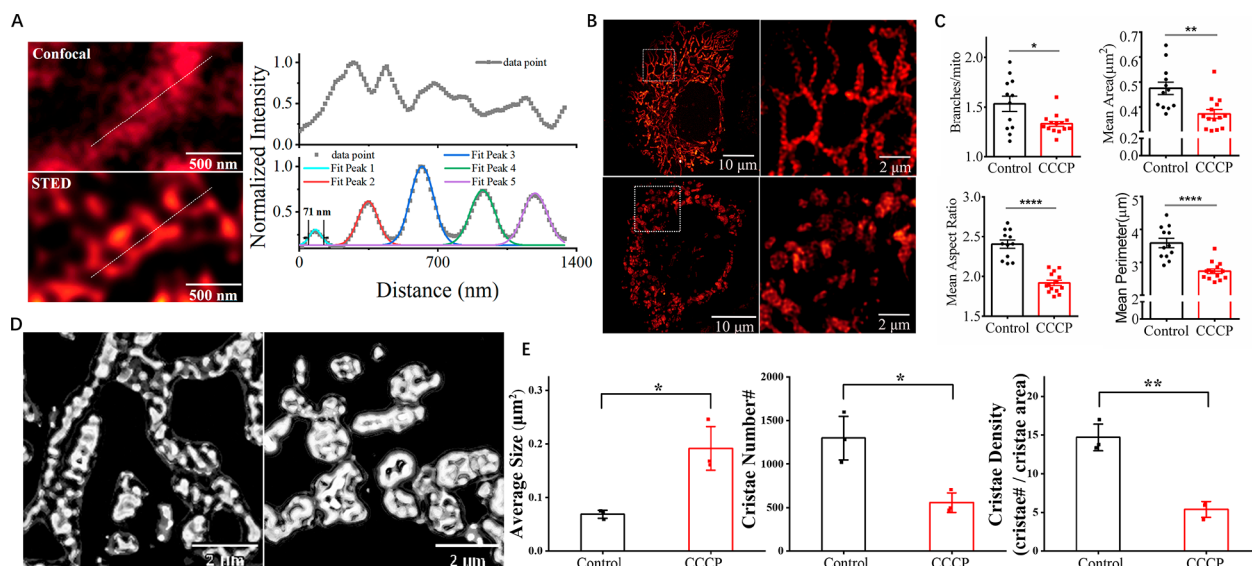

Figure 7. STED imaging of mitochondrial cristae and quantification analysis. (A) Confocal and deconvoluted STED imaging of HeLa cells expressing Cox8a-HaloTag7 incubated with 1 μM 18 for 50 min. The right figures show a line profile across the dotted line in the left images. (B) Deconvolved STED images of HeLa cells expressing Cox8a-HaloTag7. The cells were pretreated with (bottom) or without (up) 10 μM CCCP for 2 h, and subsequently incubated with 1 μM 18 for 50 min without washing step. (C) Quantification data of individual mitochondrion. (D) Representative probability maps of cristae in the absence (left) and presence (right) of CCCP. (E) Quantification data of mitochondrial cristae. Error bars represent the standard error of the means of different images (n = 460−1600 mitochondrial cristae per image). *p < 0.05; **p < 0.01; ****p < 0.0001.

Imaging Mitochondrial Fusion and Fission. Mitochondrial fusion and fission are two important mechanisms that govern mitochondrial membrane dynamics. They act in concert to control the morphology, biogenesis, or degradation of mitochondria.[29] Disruption of these processes can cause dysfunction of mitochondria, and might lead to cancers and neurodegenerative diseases.[30] The importance of mitochondrial membrane dynamics prompted us to further explore the feasibility of using our probe to track mitochondrial fusion and fission events in live cells. The fission and fusion processes of mitochondria were closely monitored by both time-lapse confocal and STED imaging using **18**. Compared with confocal images, the STED images showed substantially improved quality, allowing us to capture multiple fusion and fission events with high resolution. In the fission process of STED images (Figure 6A, 6B), it was observed that the width of the breaking junction gradually decreased (1049 nm at 00:00 min; 619 nm at 01:43 min and 364 nm at 02:33 min). Finally, the breaking junction disappeared and two individual mitochondria with a smaller size (at 03:22 min) were produced. Compared with STED, the two mitochondria could hardly be discriminated in confocal images, evidencing the superiority of tracking mitochondrial dynamic behavior with super-resolution imaging. In addition, we applied STED to observe and analyze the detailed fusion process (Figure 6C, 6D). Initially, two mitochondria with widths of 442 and 578 nm were observed. During the fusion process, the two mitochondria were moving dynamically and positioned themselves appropriately for longitudinal merging. They moved closer and connected with each other at 02:58 min. More interactions between the two mitochondria were observed at 03:48 min. Finally at 04:13 min, they completely fused into one with a width of 1292 nm. These subtle dynamic changes were difficult to observe under normal confocal imaging conditions. Furthermore, a time-lapse STED imaging mitochondrial dynamic up to 30 min in living HeLa cells was also successfully performed (Supplementary video). Collectively, these STED imaging results proved that **18** is an excellent tool for long-term and high resolution live-cell STED imaging of mitochondrial fusion and fission dynamics.

STED Quantification of Mitochondrial Cristae. Unlike the outer mitochondrial membrane, which has a smooth structure, the inner mitochondrial membrane (IMM) is highly folded to form a cristae structure. The cristae are the primary sites for oxidative phosphorylation and ATP production. They can undergo dynamic structural changes when exposed to external stimuli. However, confocal microscopy cannot visualize cristae structures due to the diffraction limit. We next explored whether our probe could resolve the mitochondrial cristae nanostructure by STED imaging. HeLa cells were transfected with Cox8a-HaloTag7, in which Cox8a was localized into the mitochondrial inner membrane. The cells were then incubated with 1 μM **18** and directly imaged with STED or confocal microscopy. As shown in Figure 7A, the mitochondrial cristae structure could clearly be resolved by STED with an FWHM resolution of 71 nm, whereas it was hardly distinguishable under confocal imaging conditions. Inspired by these results, we next attempted to quantify the morphology information on mitochondria under stimuli. As shown in Figure 7B, STED images of transfected cells treated with or without CCCP (mitochondrial oxidative phosphorylation uncoupler, a mitophagy inducer) were collected using **18**. Compared with the fibrous mitochondria in the control group, the mitochondria with CCCP treatment clearly became round or punctate.

Further quantification of the individual mitochondrion showed that the branches per mitochondrion, mean area, mean aspect ratio, and mean perimeter all decreased after CCCP was added (Figure 7C). Furthermore, we quantified the cristae to clarify the in-depth mechanism underlying morphology changes of dysfunctional mitochondria. A probability map of cristae was obtained after segmentation, showing that well-defined cristae nanostructures transformed into distinct circular membranes (Figure 7D). CCCP treatment resulted in a significant increase in cristae size and a decrease in cristae number and density (Figure 7 E), implying that the cristae tend to fuse and stretch under the stress of CCCP. These results together strongly demonstrated that **18** is well suited to quantify the nanoscale morphology information on the organelles in living cells, providing a powerful tool for diagnosing organelle-related diseases, evaluating drug safety, and other applications.

CONCLUSIONS

We systematically interrogated the intramolecular spirocyclization switching mechanism by performing a detailed structure—activity relationship study on a group of rhodamine spirolactams bearing diverse structures at the spirocyclic ring. Our study revealed that, in addition to electron-withdrawing effects, several other important factors contribute to controlling the spirocyclization equilibrium: (1) Stabilization effects such as hydrogen bond effect or resonance delocalization help to shift the equilibrium toward fluorescent zwitterions upon binding to target proteins. In particular, the stabilization effect contributed by β-fluorine is well noted. (2) For the ring-opening rate, increasing the electron-withdrawing effect can accelerate the reaction rate, whereas increasing hydrophobicity exerts negative impact. (3) The turn-on fold is determined by not only the ring-opening ability but also the fluorescence background. The low pK_a value is necessary for the low background of fluorophores. Aggregate formation of fluorophores with net-neutral charge can cause a further decrease of background. MD simulation experiments and further elucidate the underlying mechanism of aggregation at the molecular level. Collectively, these interesting findings will lay down important groundwork for the future design of high-performance fluorophores for super-resolution imaging.

On the basis of our findings, we proposed an optimized rhodamine scaffold modified by 1,1,1,3,3,3-hexafluoropropan-2-amine to construct high performance self-assembling probe **18** (**Rho-2CF3**) for STED imaging. As expected, the probe showed a very large turn-on fold and fast labeling kinetics toward Halotag7 *in vitro*, proving the feasibility of our design strategy by optimizing various factors (pK_a, stabilization effect, *etc.*). Subsequently, the probe also exhibited extraordinary properties in no-wash live-cell confocal imaging, as evidenced by their high signal-to-noise ratio, high specificity, and fast labeling. Due to its excellent ring opening ability and superior labeling kinetics, **18** was selected for the high-contrast STED imaging study. The nanostructures of photosensitive mitochondria and nuclei can be clearly observed by **18** in live cells under no-wash imaging conditions. The best resolution of as low as 42.4 nm was obtained. Due to the high brightness and good photostability of **18**, low STED power can be used without causing damage to photosensitive mitochondria. The superior properties of **18** enable dynamic analysis of the fission and fusion processes of mitochondria in living cells with high temporal and spatial resolution. Furthermore, **18** enables the quantification of nanoscale mitochondrial cristae, which provides a more in-

depth mechanism for morphological changes of mitochondria during mitophagy. Our probe quantifies mitochondrial cristae change under stimuli using the self-labeling protein tag approach with STED imaging. Compared with the existing methods to quantify mitochondrial cristae,[31−35] our approach provides higher resolution than methods using probes with structured illumination microscopy (SIM). It also gives more reliable images than methods using membrane potential-dependent probes.

In summary, our strategy for fine-tuning multiple intrinsic factors offers deep insights into the controlling mechanism of rhodamine spirocyclization. Such strategy can be extended not only to other fluorophores with spirocyclization behavior but also to the design of self-assembling probes for super-resolution imaging of various biomolecules based on specific biomolecule/ligand interactions (DNA/Hoechst, tubulin/Taxol, *etc.*). The strategy is also compatible with the recently reported exchangeable HaloTag labeling method, which will further reduce photobleaching and enable long-term super-resolution imaging.[36,37] We envision our strategy will inspire the creation of more innovative self-assembling fluorogenic probes for live-cell nanoscopy.

EXPERIMENTAL SECTION

***In Vitro* Experiments.** The ring-opening tests were performed with SDS and BSA respectively. For the turn-on fold test, 5 μM rhodamine spirolactam **1−18**, **2CF3-565** was incubated with 0.4% SDS or 0.4% BSA in pH 7.3 HEPES buffer at room temperature for 4 h. The fluorescent spectra were measured from 570 to 700 nm using an excitation wavelength of 530 nm.

For kinetic testing, 5 μM rhodamine spirolactam **2, 5, 7, 8, 2CF3-565** was incubated with 0.4% SDS in pH 7.3 HEPES buffer at room temperature. The fluorescent signal of each sample at 585 nm was measured using an excitation wavelength of 530 nm. For the pK_a test, 5 μM rhodamine spirolactam **1−18**, **2CF3-565** was incubated in Britton−Robinson buffer (pH 2 to 12) at room temperature for 2 h. The fluorescent signal of each sample at 585 nm was measured using an excitation wavelength of 530 nm.

For the size distribution test, 5 μM corresponding rhodamine spirolactam treated with or without 0.4% SDS in pH 7.3 HEPES buffer was used for transmission electron microscopy (TEM) and dynamic laser scattering (DLS) tests.

For self-labeling testing with HaloTag7, **JF525-Halo**, **16−18** was incubated with 2 equiv of HaloTag7 in pH 7.3 HEPES buffer at room temperature for 30 min. The fluorescent signals were measured from 535 to 700 nm using an excitation wavelength of 495 nm (for **JF525-Halo**) or from 570 to 700 nm using an excitation wavelength of 530 nm (for **16−18**). For protein labeling kinetic testing, 1 μM **16−18** was incubated with 1.68 μM HaloTag7 in pH 7.3 HEPES buffer at room temperature. The fluorescent signal of each sample at 585 nm was measured using an excitation wavelength of 530 nm.

Expression and Purification of HaloTag7. E. *coli* BL21 (DE3) cells transformed with plasmid pET51b-His-TEV-HaloTag7 (The plasmid was a gift from Kai Johnsson, Addgene plasmid # 167266)[27] were streaked on LB agar plates (containing 100 μg/mL Kanamycin) and grown overnight at 37 °C. A single colony was inoculated in LB media (50 mL,100 μg/mL Kanamycin) and grown with agitation (200 rpm) at 37 °C for 16 h. This culture was inoculated in LB media (1 L, 100 μg/mL Kanamycin) and then grown at 37 °C to an OD$_{600}$ of 0.6 to 0.8. Subsequently, the temperature was cooled to 28 °C. IPTG (final concentration = 1 mM) was added, and the protein was expressed for 12 h. The cells were harvested by centrifugation (4000 rpm) at 4 °C for 20 min, resuspended in TES buffer, and lysed by sonication. The supernatant was obtained by centrifugation (12000 rpm) at 4 °C for 30 min and passed through a column with purification resin (complete His-Tag). The resin was washed with Na$_2$HPO$_4$ buffer (50 mM, pH 8.0, containing 5 mM imidazole, 1 mM DTT and 300 mM NaCl) and then eluted with Na$_2$HPO$_4$ buffer (50 mM, pH 8.0, containing 250 mM imidazole, 1 mM DTT and 300 mM NaCl) according to the manufacturer's protocol. The purity of HaloTag7 was subsequently checked by SDS-PAGE analysis.

Cell Culture and Transfection. HeLa or HEK293T cells were cultured in DMEM (10% FBS, 100 μg/mL streptomycin and 100 units/mL penicillin) at 37 °C with 5% CO$_2$. The cell lines were split every 2−3 days. For transfection experiments, HeLa or HEK293T cells were seeded into a confocal dish and cultured to 20%−30% cell confluence. The medium was replaced with DMEM containing 10% FBS and without Penicillin and Streptomycin. The cells were then transfected using Lipofectamine 3000 (Invitrogen, USA) with plasmid H2B-HaloTag, HaloTag-GFP-Mito, and Cox8a-HaloTag7 respectively (The plasmid was a gift from James Zhe Liu, Addgene plasmid #91564; or from Michael Lampson, Addgene plasmid #67762; or from Kai Johnsson, Addgene plasmid # 175529).[38−40] Specifically, 1 μg of plasmid and 2 μL of P3000 were gently added to 75 μL of Opti-MEM medium. 3 μL of Lipo3000 were gently added to 75 μL of Opti-MEM medium. The two mixtures were then gently mixed in 1:1 ratio and incubated for 15 min. The transfection mixture was added into a cell culture dish, and the cells were further incubated at 37 °C for 6−8 h. After the medium was changed, the cells were cultured for another 30 h to express the HaloTag fusion protein.

No-Wash Live-Cell Confocal Microscopy. The transfected cells were first incubated with Hoechst (8 μM) for 10 min and washed by PBS. After PBS was removed, the cells were treated with different concentrations of probe in DMEM media (phenol red free, 10% FBS, 2 mM L-Glutamine and 1 mM pyruvate) for 40 min. The cells were imaged with a confocal microscope (Leica SPE) without a further washing step. The Hoechst channel (blue) was acquired from 420 to 475 nm (*ex.* 405 nm). The GFP channel (green) was acquired from 500 to 530 nm (*ex.* 488 nm). The probes channel (red) was acquired from 550 to 620 nm (*ex.* 532 nm). The Structural SIMilarity was analyzed by ImageJ plugin: SSIM index.[41,42]

No-Wash Live-Cell STED Nanoscopy. For STED imaging, about 8 × 10^4 transfected cells (transfection for 24 h) were seeded on 8-well chambered cover glass (ThermoFisher Scientific). After seeding on the cover glass for 24 h, the cells were briefly washed by DMEM (Hyclone, SH30284), and the probe diluted in DMEM was added to the cover glass. After incubation with the probe, the cells were imaged with a Leica TCS SP8 STED 3X system at room temperature. A 660 nm pulsed STED depletion laser and a 100× oil-immersion objective (Leica, N.A. 1.4) were employed in the STED imaging experiment. For STED imaging deconvolution (dSTED), the embedded Huygens Professional Software in Leica TCS SP8 STED 3X system was used. A standard unsupervised profile of Deconvolution Express tool was used to automatically find the optimal deconvolution method for each image. The spatial resolution was estimated by ImageJ plugin: Image Decorrelation Analysis.[43] The quantification data of mitochondria and cristae were analyzed by ImageJ plugin: Mitochondria Analyzer[44] or Trainable Weka Segmentation.[45,46]

ASSOCIATED CONTENT

Ⓢ Supporting Information

The Supporting Information is available free of charge at https://pubs.acs.org/doi/10.1021/acsnano.2c10467.

Synthesis and additional experimental methods; Supplementary schemes, figures, and tables; *in vitro* test; cell microscopy; NMR and HRMS spectra (PDF)

Time-lapsed STED imaging of mitochondrial fission in living HeLa cells (AVI)

Time-lapsed STED imaging of mitochondrial fusion in living HeLa cells (AVI)

Time-lapsed STED imaging of mitochondrial dynamic up to 30 min in living HeLa cells (AVI)

AUTHOR INFORMATION

Corresponding Authors

Jufang He — *Departments of Neuroscience and Biomedical Sciences, City University of Hong Kong, Hong Kong 999077, China; Centre for Regenerative Medicine and Health, Hong Kong Institute of Science and Innovation, Chinese Academy of Sciences, Hong Kong 999077, China;* Email: jufanghe@cityu.edu.hk

Hongyan Sun — *Department of Chemistry and COSDAF (Centre of Super-Diamond and Advanced Films), City University of Hong Kong, Hong Kong 999077, China;* orcid.org/0000-0003-0932-6405; Email: hongysun@cityu.edu.hk

Authors

Jie Zhang — *Department of Chemistry and COSDAF (Centre of Super-Diamond and Advanced Films), City University of Hong Kong, Hong Kong 999077, China; Centre for Regenerative Medicine and Health, Hong Kong Institute of Science and Innovation, Chinese Academy of Sciences, Hong Kong 999077, China*

Heng Shi — *Departments of Neuroscience and Biomedical Sciences, City University of Hong Kong, Hong Kong 999077, China; Guangdong Provincial Key Laboratory of Stem Cell and Regenerative Medicine, Guangzhou Institutes of Biomedicine and Health, Chinese Academy of Sciences, Guangzhou, Guangdong Province 510530, China*

Chen Huang — *Department of Chemistry and COSDAF (Centre of Super-Diamond and Advanced Films), City University of Hong Kong, Hong Kong 999077, China*

Le Mei — *Department of Chemistry and COSDAF (Centre of Super-Diamond and Advanced Films), City University of Hong Kong, Hong Kong 999077, China*

Qiang Guo — *Department of Chemistry and COSDAF (Centre of Super-Diamond and Advanced Films), City University of Hong Kong, Hong Kong 999077, China; Department of Science, School of Science and Technology, Hong Kong Metropolitan University, Hong Kong SAR 999077, China*

Ke Cheng — *Department of Chemistry and COSDAF (Centre of Super-Diamond and Advanced Films), City University of Hong Kong, Hong Kong 999077, China*

Pingzhou Wu — *Department of Chemistry and COSDAF (Centre of Super-Diamond and Advanced Films), City University of Hong Kong, Hong Kong 999077, China*

Dan Su — *Departments of Neuroscience and Biomedical Sciences, City University of Hong Kong, Hong Kong 999077, China*

Qingxin Chen — *Department of Chemistry and COSDAF (Centre of Super-Diamond and Advanced Films), City University of Hong Kong, Hong Kong 999077, China*

Shenglong Gan — *Department of Chemistry and COSDAF (Centre of Super-Diamond and Advanced Films), City University of Hong Kong, Hong Kong 999077, China*

Cecilia Ka Wing Chan — *Department of Biomedical Engineering, The Chinese University of Hong Kong, Hong Kong 999077, China;* orcid.org/0000-0003-0251-3750

Jiahai Shi — *Departments of Neuroscience and Biomedical Sciences, City University of Hong Kong, Hong Kong 999077, China*

Jian Lin Chen — *Department of Science, School of Science and Technology, Hong Kong Metropolitan University, Hong Kong SAR 999077, China*

Chung Hang Jonathan Choi — *Department of Biomedical Engineering, The Chinese University of Hong Kong, Hong Kong 999077, China;* orcid.org/0000-0003-2935-7217

Shao Q. Yao — *Department of Chemistry, National University of Singapore, 117543, Singapore;* orcid.org/0000-0003-4715-769X

Xian-Kai Chen — *Department of Chemistry and COSDAF (Centre of Super-Diamond and Advanced Films), City University of Hong Kong, Hong Kong 999077, China;* orcid.org/0000-0002-8580-7246

Ben Zhong Tang — *Department of Chemistry, The Hong Kong University of Science and Technology, Hong Kong 999077, China;* orcid.org/0000-0002-0293-964X

Complete contact information is available at:
https://pubs.acs.org/10.1021/acsnano.2c10467

Author Contributions

△J.Z. and H.S. contributed equally.

Notes

The authors declare no competing financial interest.

REFERENCES

(1) Specht, E. A.; Braselmann, E.; Palmer, A. E. A Critical and Comparative Review of Fluorescent Tools for Live-Cell Imaging. *Annu. Rev. Physiol.* **2017**, *79*, 93−117.

(2) Beija, M.; Afonso, C. A.; Martinho, J. M. Synthesis and Applications of Rhodamine Derivatives As Fluorescent Probes. *Chem. Soc. Rev.* **2009**, *38*, 2410−2433.

(3) Lavis, L. D. Teaching Old Dyes New Tricks: Biological Probes Built from Fluoresceins and Rhodamines. *Annu. Rev. Biochem.* **2017**, *86*, 825−843.

(4) Wang, L.; Frei, M. S.; Salim, A.; Johnsson, K. Small-Molecule Fluorescent Probes for Live-Cell Super-Resolution Microscopy. *J. Am. Chem. Soc.* **2019**, *141*, 2770−2781.

(5) Chi, W.; Qi, Q.; Lee, R.; Xu, Z.; Liu, X. A Unified Push−Pull Model for Understanding the Ring-Opening Mechanism of Rhodamine Dyes. *J. Phys. Chem. C* **2020**, *124*, 3793−3801.

(6) Lukinavičius, G.; Umezawa, K.; Olivier, N.; Honigmann, A.; Yang, G.; Plass, T.; Mueller, V.; Reymond, L.; Corrêa, I. R., Jr.; Luo, Z.-G. A Near-Infrared Fluorophore for Live-Cell Super-Resolution Microscopy of Cellular Proteins. *Nat. Chem.* **2013**, *5*, 132−139.

(7) Lukinavičius, G.; Reymond, L.; D'este, E.; Masharina, A.; Göttfert, F.; Ta, H.; Güther, A.; Fournier, M.; Rizzo, S.; Waldmann, H. Fluorogenic Probes for Live-Cell Imaging of The Cytoskeleton. *Nat. Methods* **2014**, *11*, 731−733.

(8) Lukinavičius, G.; Blaukopf, C.; Pershagen, E.; Schena, A.; Reymond, L.; Derivery, E.; Gonzalez-Gaitan, M.; D'Este, E.; Hell, S. W.; Gerlich, D. W. SiR−Hoechst Is a Far-Red DNA Stain for Live-Cell Nanoscopy. *Nat. Commun.* **2015**, *6*, 1−7.

(9) Lukinavičius, G.; Reymond, L.; Umezawa, K.; Sallin, O.; D'Este, E.; Göttfert, F.; Ta, H.; Hell, S. W.; Urano, Y.; Johnsson, K. Fluorogenic Probes for Multicolor Imaging in Living Cells. *J. Am. Chem. Soc.* **2016**, *138*, 9365−9368.

(10) Wirth, R.; Gao, P.; Nienhaus, G. U.; Sunbul, M.; Jäschke, A. SiRA: a Silicon Rhodamine-Binding Aptamer for Live-Cell Super-Resolution RNA Imaging. *J. Am. Chem. Soc.* **2019**, *141*, 7562−7571.

(11) Karch, S.; Broichhagen, J.; Schneider, J.; Böning, D.; Hartmann, S.; Schmid, B.; Tripal, P.; Palmisano, R.; Alzheimer, C.; Johnsson, K.; Huth, T. A New Fluorogenic Small-Molecule Labeling Tool for Surface Diffusion Analysis and Advanced Fluorescence Imaging of β-Site Amyloid Precursor Protein-Cleaving Enzyme 1 Based on Silicone Rhodamine: SiR-BACE1. *J. Med. Chem.* **2018**, *61*, 6121−6139.

(12) Butkevich, A. N.; Mitronova, G. Y.; Sidenstein, S. C.; Klocke, J. L.; Kamin, D.; Meineke, D. N.; D'Este, E.; Kraemer, P. T.; Danzl, J. G.; Belov, V. N.; Hell, S. W. Fluorescent Rhodamines and Fluorogenic Carbopyronines for Super-Resolution STED Microscopy in Living Cells. *Angew. Chem., Int. Ed.* **2016**, *55*, 3290−3294.

(13) Lukinavičius, G.; Mitronova, G. Y.; Schnorrenberg, S.; Butkevich, A. N.; Barthel, H.; Belov, V. N.; Hell, S. W. Fluorescent Dyes and Probes for Super-Resolution Microscopy of Microtubules and Tracheoles in Living Cells and Tissues. *Chem. Sci.* **2018**, *9*, 3324−3334.

(14) Zheng, Q.; Ayala, A. X.; Chung, I.; Weigel, A. V.; Ranjan, A.; Falco, N.; Grimm, J. B.; Tkachuk, A. N.; Wu, C.; Lippincott-Schwartz, J. Rational Design of Fluorogenic and Spontaneously Blinking Labels for Super-Resolution Imaging. *ACS Cent. Sci.* **2019**, *5*, 1602−1613.

(15) Grimm, J. B.; Muthusamy, A. K.; Liang, Y.; Brown, T. A.; Lemon, W. C.; Patel, R.; Lu, R.; Macklin, J. J.; Keller, P. J.; Ji, N.; Lavis, L. D. A General Method to Fine-Tune Fluorophores for Live-Cell and in Vivo Imaging. *Nat. Methods* **2017**, *14*, 987−994.

(16) Grimm, J. B.; Tkachuk, A. N.; Xie, L.; Choi, H.; Mohar, B.; Falco, N.; Schaefer, K.; Patel, R.; Zheng, Q.; Liu, Z. A General Method to Optimize and Functionalize Red-Shifted Rhodamine Dyes. *Nat. Methods* **2020**, *17*, 815−821.

(17) Koide, Y.; Urano, Y.; Hanaoka, K.; Terai, T.; Nagano, T. Evolution of Group 14 Rhodamines As Platforms for Near-Infrared Fluorescence Probes Utilizing Photoinduced Electron Transfer. *ACS Chem. Biol.* **2011**, *6*, 600−608.

(18) Umezawa, K.; Yoshida, M.; Kamiya, M.; Yamasoba, T.; Urano, Y. Rational Design of Reversible Fluorescent Probes for Live-Cell Imaging and Quantification of Fast Glutathione Dynamics. *Nat. Chem.* **2017**, *9*, 279−286.

(19) Umezawa, K.; Kamiya, M.; Urano, Y. A Reversible Fluorescent Probe for Real-Time Live-Cell Imaging and Quantification of Endogenous Hydropolysulfides. *Angew. Chem., Int. Ed.* **2018**, *57*, 9346−9350.

(20) Grzybowski, M.; Taki, M.; Senda, K.; Sato, Y.; Ariyoshi, T.; Okada, Y.; Kawakami, R.; Imamura, T.; Yamaguchi, S. A Highly Photostable Near-Infrared Labeling Agent Based on a Phospha-Rhodamine for Long-Term and Deep Imaging. *Angew. Chem., Int. Ed.* **2018**, *57*, 10137−10141.

(21) Wang, L.; Tran, M.; D'Este, E.; Roberti, J.; Koch, B.; Xue, L.; Johnsson, K. A General Strategy to Develop Cell Permeable and Fluorogenic Probes for Multicolour Nanoscopy. *Nat. Chem.* **2020**, *12*, 165−172.

(22) Lardon, N.; Wang, L.; Tschanz, A.; Hoess, P.; Tran, M.; D'Este, E.; Ries, J.; Johnsson, K. Systematic Tuning of Rhodamine Spirocyclization for Super-Resolution Microscopy. *J. Am. Chem. Soc.* **2021**, *143*, 14592−14600.

(23) Ye, Z.; Yu, H.; Yang, W.; Zheng, Y.; Li, N.; Bian, H.; Wang, Z.; Liu, Q.; Song, Y.; Zhang, M.; Xiao, Y. Strategy to Lengthen the On-Time of Photochromic Rhodamine Spirolactam for Super-Resolution Photoactivated Localization Microscopy. *J. Am. Chem. Soc.* **2019**, *141*, 6527−6536.

(24) Warren, I. D.; Wilson, E. B. Microwave Spectrum and Intramolecular Hydrogen Bonding in Trifluoroethylamine. *J. Chem. Phys.* **1972**, *56*, 2137−2141.

(25) Los, G. V.; Encell, L. P.; McDougall, M. G.; Hartzell, D. D.; Karassina, N.; Zimprich, C.; Wood, M. G.; Learish, R.; Ohana, R. F.; Urh, M. HaloTag: a Novel Protein Labeling Technology for Cell Imaging and Protein Analysis. *ACS Chem. Biol.* **2008**, *3*, 373−382.

(26) Xue, L.; Karpenko, I. A.; Hiblot, J.; Johnsson, K. Imaging and Manipulating Proteins in Live Cells Through Covalent Labeling. *Nat. Chem. Biol.* **2015**, *11*, 917−923.

(27) Wilhelm, J.; Kühn, S.; Tarnawski, M.; Gotthard, G.; Tünnermann, J.; Tänzer, T.; Karpenko, J.; Mertes, N.; Xue, L.; Uhrig, U. Kinetic and Structural Characterization of the Self-Labeling Protein Tags HaloTag7, SNAP-tag, and CLIP-tag. *Biochemistry* **2021**, *60*, 2560−2575.

(28) Hell, S. W.; Wichmann, J. Breaking the Diffraction Resolution Limit by Stimulated Emission: Stimulated-Emission-Depletion Fluorescence Microscopy. *Opt. Lett.* **1994**, *19*, 780−782.

(29) Detmer, S. A.; Chan, D. C. Functions and Dysfunctions of Mitochondrial Dynamics. *Nat. Rev. Mol. Cell Biol.* **2007**, *8*, 870−879.

(30) Giacomello, M.; Pyakurel, A.; Glytsou, C.; Scorrano, L. The Cell Biology of Mitochondrial Membrane Dynamics. *Nat. Rev. Mol. Cell Biol.* **2020**, *21*, 204−224.

(31) Shao, X.; Chen, Q.; Hu, L.; Tian, Z.; Liu, L.; Liu, F.; Wang, F.; Ling, P.; Mao, Z.-W.; Diao, J. Super-Resolution Quantification of Nanoscale Damage to Mitochondria in Live Cells. *Nano Res.* **2020**, *13*, 2149−2155.

(32) Liu, W.; Qiao, Q.; Zheng, J.; Chen, J.; Zhou, W.; Xu, N.; Li, J.; Miao, L.; Xu, Z. An Assembly-Regulated SNAP-Tag Fluorogenic Probe for Long-Term Super-Resolution Imaging of Mitochondrial Dynamics. *Biosens. Bioelectron.* **2021**, *176*, 112886.

(33) Wang, C.; Taki, M.; Sato, Y.; Tamura, Y.; Yaginuma, H.; Okada, Y.; Yamaguchi, S. A Photostable Fluorescent Marker for the Superresolution Live Imaging of the Dynamic Structure of the Mitochondrial Cristae. *Proc. Natl. Acad. Sci. U. S. A.* **2019**, *116*, 15817−15822.

(34) Zhu, T.; Yang, G.; Liu, X.; Xiang, P.; Yang, Z.; Zhang, S.; Chen, J.; Wang, H.; de Souza, S. C.; Zhang, Z. Live Cell Mitochondrial 3-Dimensional Dynamic Ultrastructures Under Oxidative Phosphorylation Revealed by a Pyridine-BODIPY Probe. *Biosens. Bioelectron.* **2021**, *178*, 113036.

(35) Yang, X.; Yang, Z.; Wu, Z.; He, Y.; Shan, C.; Chai, P.; Ma, C.; Tian, M.; Teng, J.; Jin, D. Mitochondrial Dynamics Quantitatively Revealed by STED Nanoscopy With an Enhanced Squaraine Variant Probe. *Nat. Commun.* **2020**, *11*, 1−9.

(36) Kompa, J.; Bruins, J.; Glogger, M.; Wilhelm, J.; Frei, M. S.; Tarnawski, M.; D'Este, E.; Heilemann, M.; Hiblot, J.; Johnsson, K. Exchangeable HaloTag Ligands for Super-Resolution Fluorescence Microscopy. *J. Am. Chem. Soc.* **2023**, DOI: 10.1021/jacs.2c11969.

(37) Glogger, M.; Wang, D.; Kompa, J.; Balakrishnan, A.; Hiblot, J.; Barth, H.-D.; Johnsson, K.; Heilemann, M. Synergizing Exchangeable Fluorophore Labels for Multitarget STED Microscopy. *ACS Nano* **2022**, *16*, 17991−17997.

(38) Li, L.; Liu, H.; Dong, P.; Li, D.; Legant, W. R.; Grimm, J. B.; Lavis, L. D.; Betzig, E.; Tjian, R.; Liu, Z. Real-Time Imaging of Huntingtin Aggregates Diverting Target Search and Gene Transcription. *eLife* **2016**, *5*, No. e17056.

(39) Ballister, E. R.; Ayloo, S.; Chenoweth, D. M.; Lampson, M. A.; Holzbaur, E. L. Optogenetic Control of Organelle Transport Using a Photocaged Chemical Inducer of Dimerization. *Curr. Biol.* **2015**, *25*, R407−R408.

(40) Frei, M. S.; Tarnawski, M.; Roberti, M. J.; Koch, B.; Hiblot, J.; Johnsson, K. Engineered HaloTag Variants for Fluorescence Lifetime Multiplexing. *Nat. Methods* **2022**, *19*, 65−70.

(41) Wang, Z.; Bovik, A. C.; Sheikh, H. R.; Simoncelli, E. P. Image Quality Assessment: From Error Visibility to Structural Similarity. *IEEE Trans. Image Processing* **2004**, *13*, 600−612.

(42) Prieto, G.; Chevalier, M.; Guibelalde, E. *SSIM Index As a Java Plugin for ImageJ.*. Department of Radiology, Faculty of Medicine. Universidad Complutense. Madrid. SPAIN. https://www.ucm.es/gabriel_prieto/ssim-java-and-class. December 7, 2008.

(43) Descloux, A.; Grußmayer, K. S.; Radenovic, A. Parameter-Free Image Resolution Estimation Based on Decorrelation Analysis. *Nat. Methods* **2019**, *16*, 918−924.

(44) Hemel, I. M.; Engelen, B. P.; Luber, N.; Gerards, M. A Hitchhiker's Guide to Mitochondrial Quantification. *Mitochondrion* **2021**, *59*, 216−224.

(45) Arganda-Carreras, I.; Kaynig, V.; Rueden, C.; Eliceiri, K. W.; Schindelin, J.; Cardona, A.; Sebastian Seung, H. Trainable Weka Segmentation: a Machine Learning Tool for Microscopy Pixel Classification. *Bioinformatics* **2017**, *33*, 2424−2426.

(46) Segawa, M.; Wolf, D. M.; Hultgren, N. W.; Williams, D. S.; van der Bliek, A. M.; Shackelford, D. B.; Liesa, M.; Shirihai, O. S. Quantification of Cristae Architecture Reveals Time-Dependent Characteristics of Individual Mitochondria. *Life Sci. Alliance* **2020**, *3*, No. e201900620.

⬚ Recommended by ACS